


RESEARCH ARTICLE | MARCH 02 2022

Effects of the Coriolis force in inhomogeneous rotating turbulence

Running Hu (胡润宁); Xinliang Li (李新亮) ; Changping Yu (于长平) 



Physics of Fluids 34, 035108 (2022)

<https://doi.org/10.1063/5.0084098>



View
Online



Export
Citation

CrossMark

Articles You May Be Interested In

The Coriolis field

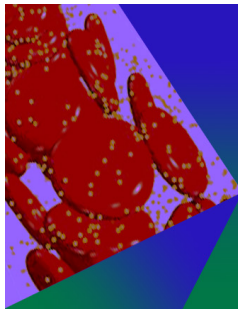
American Journal of Physics (May 2016)

Measurement of Coriolis Acceleration with a Smartphone

The Physics Teacher (May 2016)

On the Demonstration and Interpretation of the Coriolis Effect

American Journal of Physics (February 1973)



Physics of Fluids

Special Topic: Flow and Forensics

Submit Today!

 AIP
Publishing

 AIP
Publishing

Effects of the Coriolis force in inhomogeneous rotating turbulence

Cite as: Phys. Fluids **34**, 035108 (2022); doi: [10.1063/5.0084098](https://doi.org/10.1063/5.0084098)

Submitted: 3 January 2022 · Accepted: 19 February 2022 ·

Published Online: 2 March 2022





View Online



Export Citation



CrossMark

Running Hu (胡润宁),^{1,2} Xinliang Li (李新亮),^{1,2}  and Changping Yu (于长平)^{1,a)} 

AFFILIATIONS

¹State Key Laboratory of High Temperature Gas Dynamics, Institute of Mechanics, Chinese Academy of Sciences, Beijing 100190, China

²School of Engineering Science, University of Chinese Academy of Sciences, Beijing 100049, China

^{a)} Author to whom correspondence should be addressed: cpyu@imech.ac.cn

ABSTRACT

The effects of the Coriolis force in inhomogeneous rotating turbulence are studied in the paper. Linear analyses and numerical simulations both reveal that energy is transported to the slowly rotating fields, and the energy distribution is proportional to $\Omega_3^{-2}(x_3)$. The scale energy is almost spatially self-similar, and the inverse cascade is reduced by inhomogeneous rotation. The corresponding evolution equation of the scale energy, i.e., the generalized Kolmogorov equation, is calculated to study the scale transport process in the presence of inhomogeneity. The equation is reduced to twice the energy transport equation at sufficiently large scales, which is verified by numerical results. In addition, the results reveal the dominant role of the corresponding pressure of the Coriolis force in the spatial energy transport. An extra turbulent convection effect in r -space solely in slowly rotating fields is also recognized. It can be associated with the small-scale structures with strong negative vorticity, whose formation mechanism is similar to rotating condensates. Finally, by vortex dynamic analyses, we find that the corresponding pressure of the Coriolis force transports energy by vorticity tube shrinking and thickening. The effects of the Coriolis force can be divided into two components: one is related to the gradient of rotation, and the other is associated with the strength of rotation.

Published under an exclusive license by AIP Publishing. <https://doi.org/10.1063/5.0084098>

I. INTRODUCTION

Rotation is widespread in geophysical,¹ astrophysical,² and industrial flows.³ Previous studies focus on rotating flows with constant⁴ or unsteady rotation rates.⁵ However, inhomogeneous rotation is ubiquitous in natural flows, such as cyclones and anticyclones,⁶ tornadoes,¹ β planes,⁷ and quasi-Keplerian flows.^{8–10} In the β plane, the Coriolis parameter varies approximately linearly with respect to latitudes.^{11,12} The quasi-Keplerian flow is defined as the rotating flow with its specific angular momentum and angular velocity, respectively, increasing and decreasing in the radial direction.⁸

In homogeneous rotating turbulence, the rotation has been extensively investigated by researchers.^{13–16} As rotation is strengthened, the forward cascade is reduced, while the inverse cascade is intensified.^{13,17–20} By the resonant wave theory,²¹ the nonlinear triadic interactions can be divided into two categories due to their resonant properties. Using an instability hypothesis, Waleffe²¹ argued that resonant triadic interactions drive the flow to become quasi-two-dimensional. By numerical simulation, Chen *et al.*¹⁸ verified the prediction of Waleffe,²¹ and they also revealed that through non-resonant triadic interactions, energy is transferred to slow modes, i.e., the modes

of $k_z = 0$. These non-resonant triadic interactions are suppressed as the Rossby number decreases.²² Therefore, the flows with smaller Rossby numbers need more time to reach the steady state. Moreover, Yokoyama and Takaoka²³ introduced two ansatzes, net locality and efficiency of the nonlinear energy transfer, and proposed a way to determine the energy-flux vectors in homogeneous rotating turbulence. By the energy-flux vectors, Yokoyama and Takaoka²³ verified the prediction of the weak turbulence theory, and they also associated the inverse cascade with the quasi-two-dimensionalization. The cascades above also imply that the energy dissipation is suppressed by rotation, and energy piles up at large scales, which leads to condensates. Condensates have two distinct mechanisms:²⁴ rotating condensates and viscous condensates. Rotating condensates are associated with the breaking of the two-dimensionalization condition, while viscous condensates are similar to the saturation mechanism in two-dimensional flows. Seshasayanan and Alexakis²⁴ further sketched the phase space diagram of the condensates in the Re , Ro parameter plane. As for the scaling laws, Zhou²⁵ derived a spectrum of k^{-2} by phenomenological models, which is supported by simulations^{26,27} and experiments.²⁸ However, wave turbulence theories²⁹ and large eddy

simulations³⁰ both suggested that the spectrum of k^{-3} will be reached in the limit of large Reynolds numbers, small Rossby numbers, and long times.

Considering the presence of spatial transports induced by inhomogeneous rotation, a more general approach is necessary to describe the scale dynamics. The second-order structure function could be regarded as a proxy of energy associated with a given scale,^{31–37} which is also known as the scale energy. Therefore, the evolution equation of the second-order structure function can be used to depict the flux interchange between given scales as well as positions.³² The equation was discussed in detail and extended to higher orders by Hill.³¹ Since the equation can be reduced to the Kolmogorov equation in homogeneous isotropic turbulence, it is also known as the generalized Kolmogorov equation (GKE). The GKE was also applied to turbulent channel flows^{33,37} for the energy transfer in physical and r -space. Cimarelli *et al.*³⁴ further identified two dynamic processes as driving mechanisms for the energy fluxes: one in the near-wall region and another one further away from the wall. The former is related to the near-wall turbulence regeneration cycle, and the second suggests an outer self-sustaining mechanism. They³⁴ also proposed a simple equation that could capture most of the rich dynamics. Recently, the GKE was used to describe the scale-by-scale dynamics in wall flows with separation and reattachment.^{35,37}

The paper is organized as follows. The Navier–Stokes (N–S) equations in the inhomogeneous rotating frame are discussed in Sec. II. Furthermore, in Sec. III, we give the details of numerical simulations and verify the linear approximation. The results of the scale energy and the GKE are discussed in Sec. IV. By the GKE, the effects of inhomogeneous rotation are investigated in detail, especially those related to the Coriolis force. Next in Sec. V, we present the vortex dynamic processes associated with the spatial energy transports. Finally, conclusions will be given in Sec. VI.

II. N–S EQUATIONS IN THE INHOMOGENEOUS ROTATING FRAME

The relations of the velocity and acceleration between the rotating frame and the inertial frame are

$$\begin{cases} \mathbf{u}_I = \mathbf{u}_R + \boldsymbol{\Omega} \times \mathbf{x}, \\ \left(\frac{d\mathbf{u}}{dt}\right)_I = \left(\frac{d\mathbf{u}}{dt}\right)_R + 2\boldsymbol{\Omega} \times \mathbf{u}_R \\ \quad + \boldsymbol{\Omega} \times \boldsymbol{\Omega} \times \mathbf{x} + \frac{d\boldsymbol{\Omega}}{dt} \times \mathbf{x}, \end{cases} \quad (1)$$

where \mathbf{u} is the velocity, $\boldsymbol{\Omega}$ is the angular velocity, \mathbf{x} is the position, the subscript R represents the rotating frame, and the subscript I represents the inertial frame. In the inertial frame, the incompressible N–S equations can be written as

$$\begin{cases} \left(\frac{d\mathbf{u}}{dt}\right)_I = \mathbf{f} - \nabla p' + \nu \nabla^2 \mathbf{u}_I, \\ \nabla \cdot \mathbf{u}_I = 0, \end{cases} \quad (2)$$

where \mathbf{f} is the forcing term, p' is the pressure, and ν is the kinematic viscosity. In the inhomogeneous rotating frame with $\boldsymbol{\Omega} = \Omega_3(x_3)\mathbf{e}_3$, it can be derived from Eq. (1) that

$$\begin{cases} \nabla \cdot \mathbf{u}_I = 0, \\ \nabla^2 \mathbf{u}_I = \nabla^2 \mathbf{u}_R + \frac{\partial^2 \Omega_3}{\partial x_3^2} \mathbf{e}_3 \times \mathbf{x}, \end{cases} \quad (3)$$

where \mathbf{e}_3 is the unit vector parallel to the x_3 axis, $\boldsymbol{\Omega}$ is aligned with the x_3 axis, and only depends on x_3 .

The incompressible N–S equations in the rotating frame can be derived from Eqs. (1)–(3) as

$$\begin{cases} \frac{\partial \mathbf{u}}{\partial t} = -(\mathbf{u} \cdot \nabla) \mathbf{u} - \nabla p' + \nu \nabla^2 \mathbf{u} + \nu \frac{\partial^2 \Omega_3}{\partial x_3^2} \mathbf{e}_3 \times \mathbf{x} + \mathbf{f} \\ \quad + 2\mathbf{u} \times \boldsymbol{\Omega} - \boldsymbol{\Omega} \times (\boldsymbol{\Omega} \times \mathbf{x}) - \frac{d\boldsymbol{\Omega}}{dt} \times \mathbf{x}, \\ \nabla \cdot \mathbf{u}_I = 0, \end{cases} \quad (4)$$

where the subscript R is ignored. There are three fictitious forces: the Coriolis force $2\mathbf{u} \times \boldsymbol{\Omega}$, the centrifugal force $-\boldsymbol{\Omega} \times (\boldsymbol{\Omega} \times \mathbf{x})$, and the Euler force (i.e., the azimuthal force) $-(d\boldsymbol{\Omega}/dt) \times \mathbf{x}$.³⁸ In addition, there is also the residual viscous effect $\nu \partial^2 \Omega_3 / \partial x_3^2 \mathbf{e}_3 \times \mathbf{x}$. In homogeneous rotating turbulence, the centrifugal force is curl-free and thus can be merged with the pressure term,³⁹ and the Euler force is simply zero. However, in the inhomogeneous case with $\boldsymbol{\Omega} = \Omega_3(x_3)\mathbf{e}_3$, the centrifugal force and the Euler force is expanded, respectively, as follows:

$$\begin{aligned} -\boldsymbol{\Omega} \times (\boldsymbol{\Omega} \times \mathbf{x}) &= \frac{1}{2} \left[-\left(\frac{\partial \Omega_3^2}{\partial x_3}\right) (x_1^2 + x_2^2) \mathbf{e}_3 + \nabla (\boldsymbol{\Omega} \times \mathbf{x})^2 \right], \\ -\frac{d\boldsymbol{\Omega}}{dt} \times \mathbf{x} &= u_3 \frac{\partial \Omega_3}{\partial x_3} (x_2 \mathbf{e}_1 - x_1 \mathbf{e}_2). \end{aligned} \quad (5)$$

When a particle moves toward the field with a higher rotation rate (that is, $u_3 \partial \Omega_3 / \partial x_3 > 0$), the Euler force will suppress its rotation, which is analogous to the starting procedure ($\partial \Omega / \partial t > 0$) of a rotating system.³⁸

In cylinder coordinates $\{\rho, \phi, z\}$, the residual viscous term, the first components of the centrifugal force, and the overall Euler force can be written as

$$\begin{aligned} \nu \frac{\partial^2 \Omega_3}{\partial x_3^2} \mathbf{e}_3 \times \mathbf{x} &= \nu \frac{\partial^2 \Omega_3}{\partial x_3^2} |\mathbf{x}| \mathbf{e}_3 \times \phi, \\ -\frac{\partial \Omega_3^2}{\partial x_3} (x_1^2 + x_2^2) \mathbf{e}_3 &= -\frac{\partial \Omega_3^2}{\partial x_3} |\rho|^2 \mathbf{e}_3, \\ -\frac{d\boldsymbol{\Omega}}{dt} \times \mathbf{x} &= -u_3 \frac{\partial \Omega_3}{\partial x_3} |\rho| \phi, \end{aligned} \quad (6)$$

which introduce the influence of the radius vector ρ and the angular vector ϕ . They cannot be periodic and conflict with the boundary conditions of our simulations. Therefore, these terms are neglected for simplification.

Similar to the situation of the β plane,^{11,40} the effects of the Coriolis force are the focus. Then, the N–S equations have the same form as those in the homogeneous rotating flows,⁴¹ which can be written as

$$\begin{cases} \frac{\partial \mathbf{u}}{\partial t} = -(\mathbf{u} \cdot \nabla) \mathbf{u} - \nabla p + \nu \nabla^2 \mathbf{u} + \mathbf{f} + 2\mathbf{u} \times \boldsymbol{\Omega}, \\ \nabla \cdot \mathbf{u} = 0, \end{cases} \quad (7)$$

where p is the modified pressure including the original pressure p' and the second term of the centrifugal force in Eq. (5).

III. NUMERICAL SIMULATIONS AND LINEAR APPROXIMATION

A. Numerical setup

Three direct numerical simulations are carried out for inhomogeneous rotating flows. The triply periodic pseudo-spectral method and third-order Runge–Kutta technique are applied to the simulations. The angular velocity $\mathbf{\Omega}$ is aligned with the third direction and only relies on the coordinate of the third direction, i.e., $\mathbf{\Omega} = \Omega_3(x_3)\mathbf{e}_3$. The computational domains and meshes are doubled in the third direction, which are $[2\pi]^2 \times 4\pi$ and $1024^2 \times 2048$, respectively.

The N–S equations in the inhomogeneous rotating frame^{38,41} is given in Eq. (7). The forcing term \mathbf{f} is calculated in the Fourier space as⁴²

$$\hat{\mathbf{f}}(\mathbf{k}) = \frac{\epsilon_f \hat{\mathbf{u}}(\mathbf{k})}{[n_f \hat{\mathbf{u}}(\mathbf{k}) \cdot \hat{\mathbf{u}}(\mathbf{k})]}, \quad (8)$$

where $\hat{}$ represents the value in the Fourier space, ϵ_f is the energy injection rate, and n_f is the number of energy injection wavenumbers.

Rotating turbulence is quantified by two non-dimensional parameters: the Reynolds number Re and the Rossby number Ro . Typically, the Rossby number of the synoptic scales at mid-latitudes in the atmosphere is approximately 0.1.⁴³ The two non-dimensional parameters here can be defined as³⁹

$$Re = \epsilon_f^{1/3} k_f^{-4/3} / \nu, Ro = k_f^{2/3} \epsilon_f^{1/3} / 2\bar{\Omega}, \quad (9)$$

where $\bar{\Omega}$ is the mean rotation rate, and k_f is the forcing wavenumber.

Considering the case of the β plane¹¹ and the requirement of infinite-order smooth derivatives of the pseudo-spectral method, we suppose that the rotation rate varies along the rotating axis as

$$\Omega_3(x_3) / \bar{\Omega} = 1 - \alpha \cos(x_3/2), \quad (10)$$

where α is the variation ratio, and $x_3 \in [0, 4\pi]$.

Three cases are involved in the paper. For all the three cases, the forcing wavenumbers $k_f = \{8, 9\}$, the mean rotating rate $\bar{\Omega} = 10.42$, the kinematic viscosity $\nu = 10^{-3}$, and the energy injection rate $\epsilon_f = 0.1$. The non-dimensional parameters $Re = 26.76$ and $Ro = 0.093$. All the statistics in the paper are averaged over at least 53.6 eddy turnover times after reaching the steady state, where the eddy turnover time $T_0 = L_F/U$, the scale $L_F = 2\pi/k_f$, and the root mean square velocity $U = \sqrt{\langle u_i u_i \rangle} / \sqrt{3}$. The variation ratio α varies from 0.0 to 0.5. Notably, when $\alpha = 0.0$, the case is homogeneous. Other parameters are mentioned in Table I.

B. Structures and spectra

Figure 1 illustrates the vortex structures of all the three cases by the Q criterion. Notably, the column structures in Fig. 1(a) are thin

TABLE I. Descriptions of the data. α : the variation ratio of rotating rate; U : the root mean square velocity; T_0 : the eddy turnover time; η : the Kolmogorov dissipative scale; Δx : the numerical grid spacing; and Δt : the time increment.

Case	α	U	T_0	$\eta/\Delta x$	$U\Delta t/\Delta x$
A	0.00	1.25	0.59	1.63	0.016
B	0.25	1.16	0.64	1.63	0.015
C	0.50	1.05	0.70	1.63	0.025

and dense compared with previous results.⁴⁴ It can be attributed to the doubled domain in the third direction, which intensifies the interactions between the slow manifolds and the fast manifolds with minimum $|k_3|$ ⁴⁵ and reduces the inverse cascade. Furthermore, the upper components of Figs. 1(a)–1(c) reveal that as the variation becomes more intense, more structures with strong vorticity ($Q > 1500$) concentrate on the slowly rotating fields. The stronger the vortices are, the more interference there is among them, and thus more microvortexes (mostly with negative vorticity) form in the slowly rotating fields, as shown in the lower components of Fig. 1(c) by the red color.

Considering the spectral behaviors of inhomogeneous rotating flows, since the flows are inhomogeneous in the third direction, the Fourier transform is only performed in other two dimensions. The velocity $\mathbf{u}(k_1, k_2, x_3)$ can be calculated as

$$\mathbf{u}(k_1, k_2, x_3) = \frac{1}{N_1 N_2} \sum_{x_1} \sum_{x_2} \mathbf{u}(\mathbf{x}) \exp[-i(k_1 x_1 + k_2 x_2)], \quad (11)$$

where N_1 and N_2 are the mesh sizes of the first two dimensions, and $i = \sqrt{-1}$. Furthermore, the corresponding spectrum can be written as

$$E(k_\perp, x_3) = \frac{1}{2} \sum_{k_1^2 + k_2^2 = k_\perp^2} \mathbf{u}^*(k_1, k_2, x_3) \cdot \mathbf{u}(k_1, k_2, x_3), \quad (12)$$

where k_\perp is the wavenumber perpendicular to the rotating axis. The average spectrum over x_3 is calculated as

$$E(k_\perp) = \frac{1}{N_3} \sum_{x_3} E(k_\perp, x_3), \quad (13)$$

where N_3 is the mesh sizes of the third dimension. The average spectra over x_3 are given in Fig. 2. As the variation ratio become stronger (from case A to case C), the energy at the large scales ($k_\perp \leq 2$) is suppressed, while the energy at other scales is less affected. Moreover, in the inertial region ($20 < k_\perp < 100$), $E(k_\perp) \sim k_\perp^{-2.8}$. The spectra of case C ($\alpha = 0.5$) at different positions x_3 are shown in Fig. 3. Since the spectra are symmetric about $x_3 = 2\pi$, there are only the spectra of half domains, i.e., $x_3 \in [0, 2\pi]$. As x_3 varies from 0 to 2π , the rotation becomes stronger, the energy becomes weaker, especially the energy in the dissipative region ($k > 100$). In other words, the small-scale energy and dissipation in the slowly rotating fields are far larger than those in the fast rotating fields, which could be associated with the abundant small structures in the slowly rotating fields shown in Fig. 1(c).

C. Linear approximation

The vorticity equation can be derived from the N–S equations [Eq. (4)] as

$$\frac{\partial \boldsymbol{\omega}}{\partial t} - (\boldsymbol{\omega} \cdot \nabla) \mathbf{u} + (\mathbf{u} \cdot \nabla) \boldsymbol{\omega} = \nu \nabla^2 \boldsymbol{\omega} + \nabla \times \mathbf{f} + 2\nabla \times (\mathbf{u} \times \mathbf{\Omega}), \quad (14)$$

where the Lamb vector is used to replace the turbulent convection in the derivation, i.e., $\mathbf{u} \times \boldsymbol{\omega} = -\mathbf{u} \cdot \nabla \mathbf{u} - \nabla(\frac{1}{2}|\mathbf{u}|^2)$. Referring to the Taylor–Proudman theorem,⁴⁶ neglecting the viscous term, the forcing term, and the turbulent convection term ($Ro \ll 1$), the vorticity equation yields

$$\frac{\partial \boldsymbol{\omega}}{\partial t} = 2\nabla \times (\mathbf{u} \times \mathbf{\Omega}). \quad (15)$$

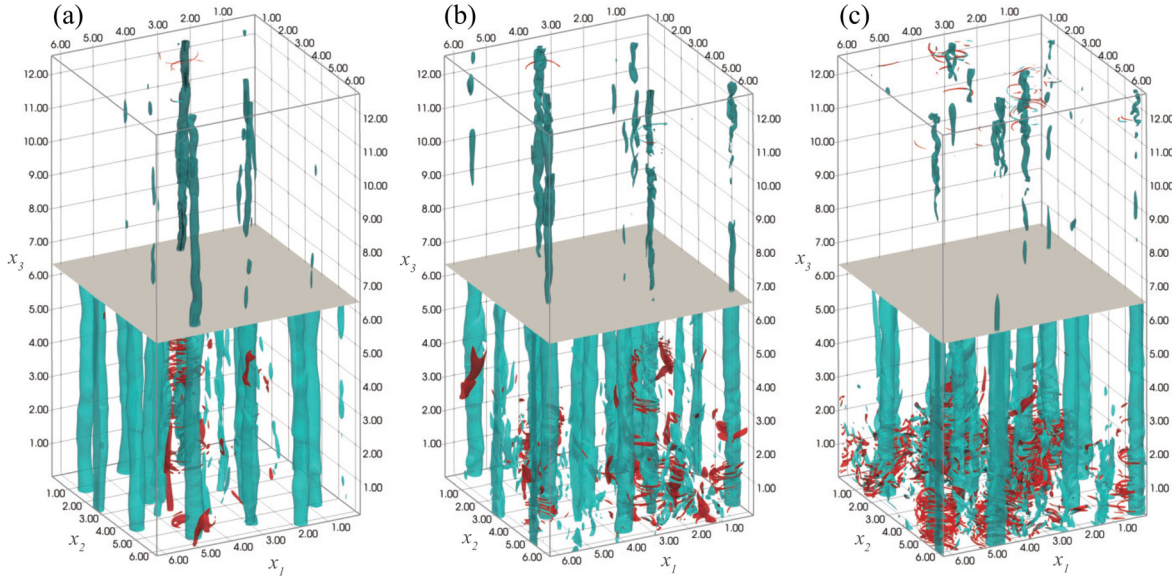


FIG. 1. 3D rendering of the vortex structures shown by the Q criterion: (a) case A, $\alpha = 0$; (b) case B, $\alpha = 0.25$; and (c) case C, $\alpha = 0.50$. Blue: $\omega_3 > 0$; red: $\omega_3 < 0$. The domain is divided into two components for each case: the upper component shows the results of $Q > 1500$, and the lower component gives the results of $Q > 100$.

If the motion is steady ($\partial/\partial t = 0$), and considering that $\mathbf{\Omega} = \Omega_3(x_3)\mathbf{e}_3$, the equation can be reduced as

$$\mathbf{0} = \frac{\partial(\Omega_3\mathbf{u})}{\partial x_3} - u_3 \frac{\partial\Omega_3}{\partial x_3} \mathbf{e}_3. \quad (16)$$

Multiplying the three components of the equation with $\{\Omega_3 u_1, \Omega_3 u_2, u_3\}$ separately and integrating in the x_3 axis, it can be deduced that $u_1^2 \Omega_3^2$, $u_2^2 \Omega_3^2$ and u_3^2 are independent of x_3 . If averaging over the $x_1 - x_2$ plane, the turbulent kinematic energy can be obtained as

$$E_{\perp}(x_3) = C_1/\Omega_3^2, \quad E_{\parallel}(x_3) = C_2, \quad (17)$$

where $E_{\perp}(x_3) = \langle u_1^2 + u_2^2 \rangle_{\perp}/2$, $E_{\parallel}(x_3) = \langle u_3^2 \rangle_{\perp}/2$, $\langle \cdot \rangle_{\perp}$ represents the average over the $x_1 - x_2$ planes, and $C_i = \text{const}$.

Figure 4 gives the energy distributions of case B and case C. Figure 4(a) gives the distribution with respect to the non-dimensional rotation rate $\Omega_3(x_3)/\bar{\Omega}$, while Fig. 4(b) takes x_3 as the abscissa. The inset of Fig. 4(b) shows the details at the region of $x_3 \in [3.5\pi, 4.0\pi]$. In Fig. 4(a), $E_{\perp}(x_3)$ fits well with Ω_3^{-2} for the two cases. This can be verified in Fig. 4(b) as well. More precisely, as shown in the inset of Fig. 4(b), for case C, when $x_3 < 0.32\pi$ or $x_3 > 3.6\pi$, $E_{\perp}(x_3)$ deviates from the prediction of the linear approximation. Moreover, $E_{\parallel}(x_3) \approx 0$, which is approximately a constant, as expected.

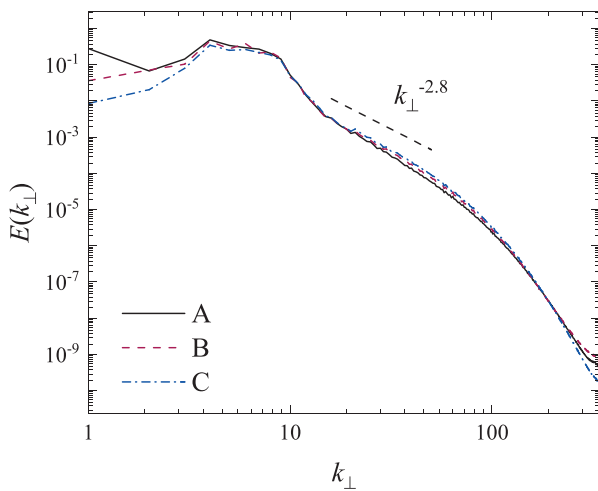


FIG. 2. The average spectra over x_3 . Dash line: $k_{\perp}^{-2.8}$.

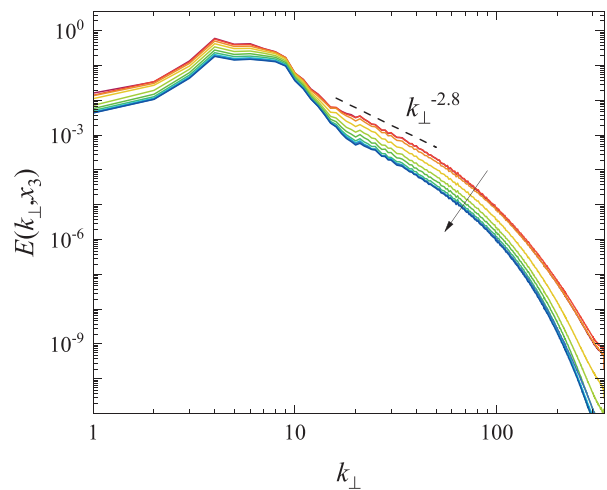


FIG. 3. The spectra with different x_3 of case C ($\alpha = 0.5$). Dash line: $k_{\perp}^{-2.8}$. In the direction of the arrow, x_3 varies from 0 to 2π , and $\Omega_3(x_3)$ increases.

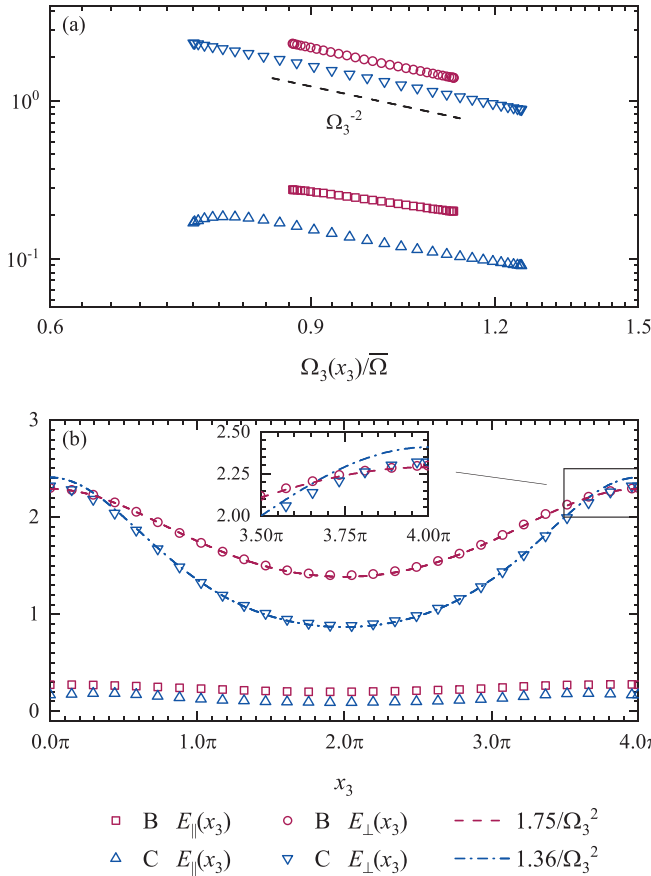


FIG. 4. Energy distributions: (a) log–log plot of $E_{\parallel}(x_3)$ and $E_{\perp}(x_3)$ with respect to $\Omega_3(x_3)/\bar{\Omega}$. Dash line: Ω_3^{-2} . (b) Plot of $E_{\parallel}(x_3)$ and $E_{\perp}(x_3)$ with respect to x_3 .

IV. THE TRANSFER PROCESSES

Since the flow is inhomogeneous in the third direction, the energy transports in geometrical space are as important as those among scales. To study them simultaneously, the second-order structure function (i.e., the scale energy) and its evolution equation (i.e., the GKE^{31–34}) are calculated.

A. Scale energy

The velocity increment at the position \mathbf{X} and separation \mathbf{r} is illustrated in Fig. 5. The velocity at two positions \mathbf{x} and \mathbf{x}' are denoted as \mathbf{u} and \mathbf{u}' , respectively. The velocity increment and scale energy at the position \mathbf{X} and separation \mathbf{r} are written as

$$\begin{aligned} \delta\mathbf{u}(\mathbf{X}, \mathbf{r}) &= \mathbf{u} - \mathbf{u}', \\ \delta u^2(\mathbf{X}, \mathbf{r}) &= \delta\mathbf{u}(\mathbf{X}, \mathbf{r}) \cdot \delta\mathbf{u}(\mathbf{X}, \mathbf{r}), \end{aligned} \tag{18}$$

where $\mathbf{X} = (\mathbf{x} + \mathbf{x}')/2$, and $\mathbf{r} = \mathbf{x} - \mathbf{x}'$. For simplification, in this paper, we only consider the separation \mathbf{r} with $r_3 = 0$. Moreover, since the flows satisfy the translation and rotation invariance on the $x_1 - x_2$ plane, the scale energy is averaged over the $x_1 - x_2$ plane and the ring of $r = |\mathbf{r}|$, i.e.,

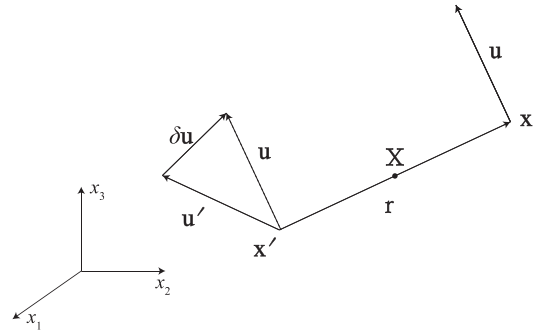


FIG. 5. Sketch of the velocity increment.

$$\langle \delta u^2 \rangle_{\perp}(x_3 = X_3, r) = \frac{1}{N_1 N_2 N_r} \sum_{X_1} \sum_{X_2} \sum_{|\mathbf{r}|=r} \delta u^2(\mathbf{X}, \mathbf{r}), \tag{19}$$

where N_r is the number of points with $|\mathbf{r}| = r$.

To exclude the influence of the amplitudes of the average energy, the normalized scale energy $\langle \delta \bar{u}^2 \rangle_{\perp}$ is calculated as

$$\langle \delta \bar{u}^2 \rangle_{\perp}(x_3, r) = \langle \delta u^2 \rangle_{\perp}(x_3, r) / E(x_3), \tag{20}$$

where $E(x_3) = E_{\parallel}(x_3) + E_{\perp}(x_3)$. When the separation $r \rightarrow \infty$, the two-point correlation of the two points \mathbf{x} and \mathbf{x}' is negligible, i.e., $\lim_{r \rightarrow \infty} \langle \mathbf{u} \cdot \mathbf{u}' \rangle_{\perp} = 0$. Furthermore, the asymptotic behavior of $\langle \delta \bar{u}^2 \rangle_{\perp}$ can be derived as

$$\lim_{r \rightarrow \infty} \langle \delta \bar{u}^2 \rangle_{\perp} = \lim_{r \rightarrow \infty} (4E - 2\langle \mathbf{u} \cdot \mathbf{u}' \rangle_{\perp}) / E = 4. \tag{21}$$

Figure 6 gives the normalized scale energy $\langle \delta \bar{u}^2 \rangle_{\perp}$. As predicted, when the separation $r \rightarrow \infty$, the normalized scale energy $\langle \delta \bar{u}^2 \rangle_{\perp}$ tends to be 4. Furthermore, in the dissipative region ($r < 0.022\pi$), $\langle \delta \bar{u}^2 \rangle_{\perp} \sim r^2$, which is consistent with the prediction of Kolmogorov.⁴⁷ $\langle \delta \bar{u}^2 \rangle_{\perp} \sim r^{1.8}$ in the inertial region ($0.03\pi < r < 0.08\pi$), which can be associated with the spectrum $E(k_{\perp}) \sim k_{\perp}^{-2.8}$.

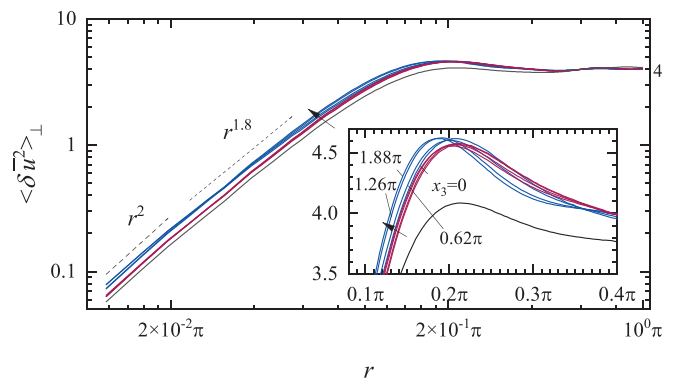


FIG. 6. The log–log plot of the normalized scale energy $\langle \delta \bar{u}^2 \rangle_{\perp}$ with respect to the separation r at different position x_3 . Black lines: case A; red lines: case B; and blue lines: case C. In the direction of the arrows, x_3 varies from 0 to 2π , and $\Omega_3(x_3)/\bar{\Omega}$ increases. The inset gives the details around the peak in linear coordinates.

Moreover, in Fig. 6, comparing the results of case C ($\alpha = 0.5$) with those of case A ($\alpha = 0.0$), the small-scale motion ($r < 0.2\pi$) of case C is intensified due to inhomogeneity. In other words, the inhomogeneity reduces the inverse cascade and intensifies the forward cascade. It is because the inhomogeneity introduces additional triadic interactions, which break the isolation of slow manifolds from other manifolds.⁴ Moreover, the normalized scale energy distributions are almost independent of x_3 , which means the scale energy is geometrically self-similar. The inset of Fig. 6 allows for finer distinctions of the results with different x_3 . As x_3 increases, the rotation becomes stronger, and the peak of scale energy slightly moves to smaller scales.

B. Energy transport equation

Before studying the scale transport process, the energy transport equation in physical space is discussed at first. To better understand the transport process, pressure decomposition⁴⁸ is needed. Taking the divergence of Eq. (7), the resulting equation is

$$\nabla^2 p = -\nabla \cdot [(\mathbf{u} \cdot \nabla)\mathbf{u}] + 2\nabla \cdot (\mathbf{u} \times \boldsymbol{\Omega}), \quad (22)$$

which means that the pressure term can be divided into two components corresponding to the turbulent convection and the Coriolis force separately, i.e., $p = p^n + p^c$. The composition of the term and the corresponding pressure term is solenoidal. It is closely related to the vortex dynamics discussed in Sec. V.

Contracting the N-S equations [Eq. (7)] with \mathbf{u} and averaging in the $x_1 - x_2$ plane lead to

$$\frac{\partial E}{\partial t} = P + \Phi + \Pi^c + \Pi^n, \quad (23)$$

where $E(x_3) = E_{\parallel}(x_3) + E_{\perp}(x_3)$. The terms on the right-hand side (RHS) are

$$P = \langle \mathbf{u} \cdot \mathbf{f} \rangle_{\perp}, \quad (24a)$$

$$\Phi = \frac{1}{2} \nu \frac{\partial^2}{\partial x_3^2} \langle \mathbf{u} \cdot \mathbf{u} \rangle_{\perp} - \nu \langle \nabla \mathbf{u} : \nabla \mathbf{u} \rangle_{\perp}, \quad (24b)$$

$$\Pi^c = -\frac{\partial}{\partial x_3} \langle u_3 p^c \rangle_{\perp}, \quad (24c)$$

$$\Pi^n = -\frac{1}{2} \frac{\partial}{\partial x_3} \langle \mathbf{u} \cdot \mathbf{u} u_3 \rangle_{\perp} - \frac{\partial}{\partial x_3} \langle u_3 p^n \rangle_{\perp}, \quad (24d)$$

where P is the production term; Φ is the viscous term, including the viscous diffusion term $\nu \partial^2 \langle \mathbf{u} \cdot \mathbf{u} \rangle_{\perp} / \partial x_3^2 / 2$ and the pseudo-dissipation term $-\nu \langle \nabla \mathbf{u} : \nabla \mathbf{u} \rangle_{\perp}$; Π^c is the Coriolis term plus the corresponding pressure term; and Π^n is the turbulent convection term plus the corresponding pressure term. In the derivation above, we use $\mathbf{u} \cdot (\mathbf{u} \times \boldsymbol{\Omega}) = 0$ and $\partial \langle \cdot \rangle_{\perp} / \partial x_1 = \partial \langle \cdot \rangle_{\perp} / \partial x_2 = 0$.

To verify the steady state, $\partial E / \partial t$ of Eq. (23) is calculated. The max value of case B $\max\{|\partial E / \partial t|\} = 0.035$ and that of case C $\max\{|\partial E / \partial t|\} = 0.020$. Since case A is homogeneous ($\alpha = 0$), the case is not discussed here. The results of case B are more difficult to reach balance than those of case C, due to the weaker variation ratio α of case B. Figure 7 presents all the terms on the RHS of Eq. (23). In both Figs. 7(a) and 7(b), $\partial E / \partial t \sim 0$, $P > 0$ and $\Phi < 0$. More specifically, in Fig. 7(a), P and Φ are approximately equal, while in Fig. 7(b), the dissipation Φ is obviously larger than the production P when $x_3 < 0.8\pi$, which can be attributed to the small vortices with negative

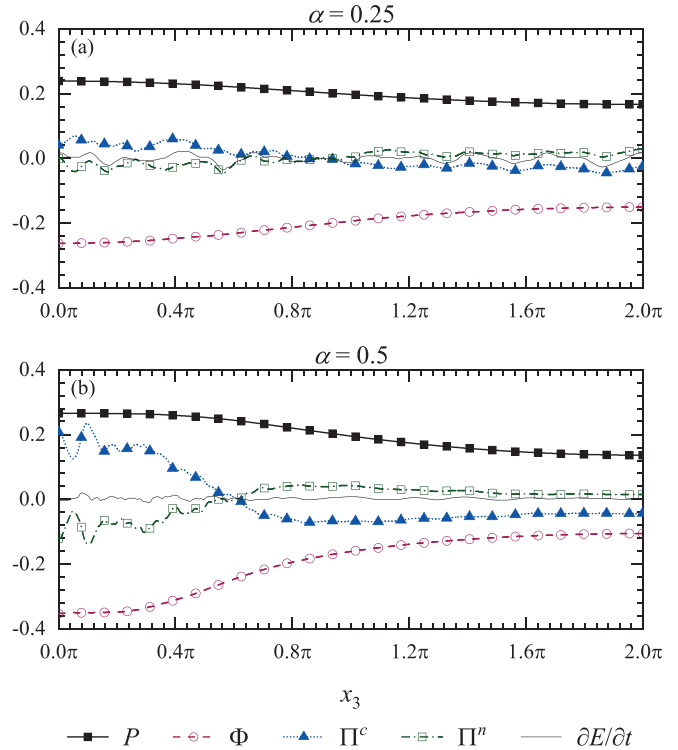


FIG. 7. All terms of the energy transport equation vs the position x_3 : (a) case B, $\alpha = 0.25$ and (b) case C, $\alpha = 0.50$. P : the production term; Φ : the viscous term; Π^c : the Coriolis term and the corresponding pressure term; and Π^n : the turbulent convection term and the corresponding pressure term.

vorticity shown in Fig. 1(c). The structures are produced by interference among adjacent columnar vortices. Additionally, in Fig. 7, Π^c transports energy from the fast rotating fields ($x_3 > 0.84\pi$ for case B and $x_3 > 0.56\pi$ for case C) to the remaining domains. In contrast, Π^n transports energy inversely due to the inhomogeneity of energy distributions.

C. The generalized Kolmogorov equation and reliability verification

According to the relationships among the partial derivatives,³¹

$$\begin{aligned} \frac{\partial}{\partial x_i} &= \frac{\partial}{\partial r_i} + \frac{1}{2} \frac{\partial}{\partial X_i}, & \frac{\partial}{\partial x'_i} &= -\frac{\partial}{\partial r_i} + \frac{1}{2} \frac{\partial}{\partial X_i}, \\ \frac{\partial}{\partial X_i} &= \frac{\partial}{\partial x_i} + \frac{\partial}{\partial x'_i}, & \frac{\partial}{\partial r_i} &= \frac{1}{2} \left(\frac{\partial}{\partial r_i} + \frac{\partial}{\partial X_i} \right), \end{aligned} \quad (25)$$

the GKE can be derived from the N-S equations [Eq. (4)] as

$$\begin{aligned} \frac{1}{2} \frac{\partial}{\partial t} \langle \delta u^2 \rangle_{\perp} &= \frac{\partial}{\partial X_3} \left\langle -\frac{1}{2} \delta u^2 u_3^* - \delta u_3 \delta p + \frac{1}{4} \nu \frac{\partial}{\partial X_3} \delta u^2 \right\rangle_{\perp} \\ &+ \nabla_{\mathbf{r}} \cdot \left\langle -\frac{1}{2} \delta \mathbf{u} \delta u^2 + \nu \nabla_{\mathbf{r}} \delta u^2 \right\rangle_{\perp} \\ &+ \langle \delta \mathbf{u} \cdot \delta \mathbf{f} \rangle_{\perp} - \langle \epsilon^* \rangle_{\perp}, \end{aligned} \quad (26)$$

where $\nabla_{\mathbf{r}} = \partial / \partial r_1 \mathbf{e}_1 + \partial / \partial r_2 \mathbf{e}_2 + \partial / \partial r_3 \mathbf{e}_3$, $*$ represents the sum at points \mathbf{x} and \mathbf{x}' , and the pseudo-dissipation $\langle \epsilon^* \rangle_{\perp} = \nu \langle \frac{\partial u_i}{\partial x_j} \frac{\partial u_i}{\partial x_j} + \frac{\partial u'_i}{\partial x'_j} \frac{\partial u'_i}{\partial x'_j} \rangle_{\perp}$.

Similar to the scale energy in Eq. (19), all the terms in Eq. (26) of separation r are averaged over the $x_1 - x_2$ plane and the ring of $r = |\mathbf{r}|$. The terms on the RHS represent the spatial transport, scale transport, production, and pseudo-dissipation in sequence. The spatial transport can be divided into the turbulent convection $-\frac{\partial}{\partial X_3} \langle \frac{1}{2} \delta u^2 u_3^* \rangle_{\perp}$, pressure transport $-\frac{\partial}{\partial X_3} \langle \delta u_3 \delta p \rangle_{\perp}$, and viscous diffusion $\frac{\partial}{\partial X_3} \langle \frac{1}{4} \nu \frac{\partial}{\partial X_3} \delta u^2 \rangle_{\perp}$. The transport in r -space includes the turbulent convection $\nabla_{\mathbf{r}} \cdot \langle -\frac{1}{2} \delta \mathbf{u} \rangle$ and viscous diffusion $\nabla_{\mathbf{r}} \cdot \langle \nu \nabla_{\mathbf{r}} \delta u^2 \rangle_{\perp}$. The decomposition of pressure [Eq. (22)] is also performed here. The pressure transport in geometrical space is divided into two components corresponding to the turbulent convection and the Coriolis force separately, i.e.,

$$-\frac{\partial}{\partial X_3} \langle \delta u_3 \delta p \rangle_{\perp} = -\frac{\partial}{\partial X_3} \langle \delta u_3 \delta p^n \rangle_{\perp} - \frac{\partial}{\partial X_3} \langle \delta u_3 \delta p^c \rangle_{\perp}. \quad (27)$$

Similar to the asymptotic behaviors of the scale energy, the asymptotic behaviors of all terms of the GKE [Eq. (26)] can be written as

$$\frac{1}{2} \lim_{r \rightarrow \infty} \langle \delta u^2 \rangle_{\perp} = \frac{1}{2} \langle \mathbf{u} \cdot \mathbf{u} \rangle_{\perp} = 2E, \quad (28a)$$

$$\lim_{r \rightarrow \infty} \langle \delta \mathbf{u} \cdot \delta \mathbf{f} \rangle_{\perp} = 2 \langle \mathbf{u} \cdot \mathbf{f} \rangle_{\perp} = 2P, \quad (28b)$$

$$\begin{aligned} \frac{1}{4} \nu \lim_{r \rightarrow \infty} \frac{\partial^2}{\partial X_3^2} \langle \delta u^2 \rangle_{\perp} + \nu \lim_{r \rightarrow \infty} \nabla_{\mathbf{r}}^2 \langle \delta u^2 \rangle_{\perp} - \lim_{r \rightarrow \infty} \langle \epsilon^* \rangle_{\perp} \\ = \nu \frac{\partial^2}{\partial x_3^2} \langle \mathbf{u} \cdot \mathbf{u} \rangle_{\perp} - 2\nu \langle \nabla \mathbf{u} : \nabla \mathbf{u} \rangle_{\perp} = 2\Phi, \end{aligned} \quad (28c)$$

$$-\lim_{r \rightarrow \infty} \frac{\partial}{\partial X_3} \langle \delta u_3 \delta p^c \rangle_{\perp} = -2 \frac{\partial}{\partial x_3} \langle u_3 p^c \rangle_{\perp} = 2\Pi^c, \quad (28d)$$

$$\begin{aligned} -\frac{1}{2} \lim_{r \rightarrow \infty} \frac{\partial}{\partial X_3} \langle \delta u^2 u_3^* \rangle_{\perp} - \frac{1}{2} \lim_{r \rightarrow \infty} \nabla_{\mathbf{r}} \cdot \langle \delta \mathbf{u} \delta u^2 \rangle_{\perp} - \lim_{r \rightarrow \infty} \frac{\partial}{\partial X_3} \langle \delta u_3 \delta p^n \rangle_{\perp} \\ = -\frac{\partial}{\partial x_3} \langle \mathbf{u} \cdot \mathbf{u} u_3 \rangle_{\perp} - 2 \frac{\partial}{\partial x_3} \langle u_3 p^n \rangle_{\perp} = 2\Pi^n. \end{aligned} \quad (28e)$$

Thus, when $r \rightarrow \infty$, the GKE is reduced to Eq. (23) $\times 2$. Figure 8 shows the results of the GKE (divided by 2) of case C at the separation $r = 0.48\pi$. The subscript k is to distinguish the terms of the GKE

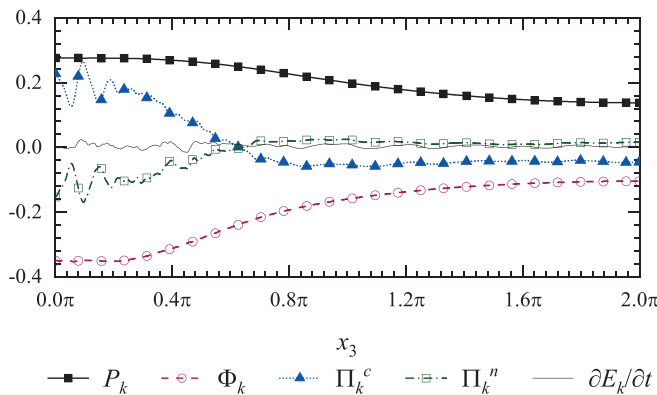


FIG. 8. All terms of the GKE (divided by two) of case C at the separation $r = 0.48\pi$. The subscript k is to distinguish with the terms of the energy transport equation.

from those of the energy transport equation. Compared with Fig. 7(b), the results are almost the same, which verify the validity of the GKE and the above prediction of the asymptotic behaviors.

There are also some relationships between the transport processes in geometrical space and r -space. For the turbulent convection in the direction of x_3 , there is a relation,

$$\begin{aligned} \lim_{r \rightarrow \infty} -\frac{1}{2} \frac{\partial}{\partial r_3} \langle \delta u_3 \delta u^2 \rangle_{\perp} &= \lim_{r \rightarrow \infty} -\frac{1}{2} \frac{\partial}{\partial X_3} \langle \delta u^2 u_3^* \rangle_{\perp} \\ &= -\frac{1}{2} \frac{\partial}{\partial x_3} \langle \mathbf{u} \cdot \mathbf{u} u_3 \rangle_{\perp}. \end{aligned} \quad (29)$$

Similarly, for the viscous diffusion, there is another equality,

$$\lim_{r \rightarrow \infty} \nu \frac{\partial^2}{\partial r_3^2} \langle \delta u^2 \rangle_{\perp} = \lim_{r \rightarrow \infty} \frac{\nu}{4} \frac{\partial^2}{\partial X_3^2} \langle \delta u^2 \rangle_{\perp} = \frac{\nu}{2} \frac{\partial^2}{\partial x_3^2} \langle \mathbf{u} \cdot \mathbf{u} \rangle_{\perp}. \quad (30)$$

Figure 9 gives the results of turbulent convection [in (a)] and viscous diffusion [in (b)] at separation $r = 0.48\pi$. As predicted, the transport terms in geometrical space and r -space are almost the same. It may be confusing that the viscous diffusion oscillates violently. This is acceptable given that viscous diffusion is two orders of magnitude less than the other terms (such as turbulent convection) at the separation $r = 0.48\pi$.

D. Transport process in r -space

The average in the r -space^{32,33} is calculated on the two-dimensional circle domains perpendicular to the rotating axis. In other words, for a generic quantity $q(r', x_3)$ at the separation r' and position x_3 , its average in the r -space $Q(r, x_3)$ is given as

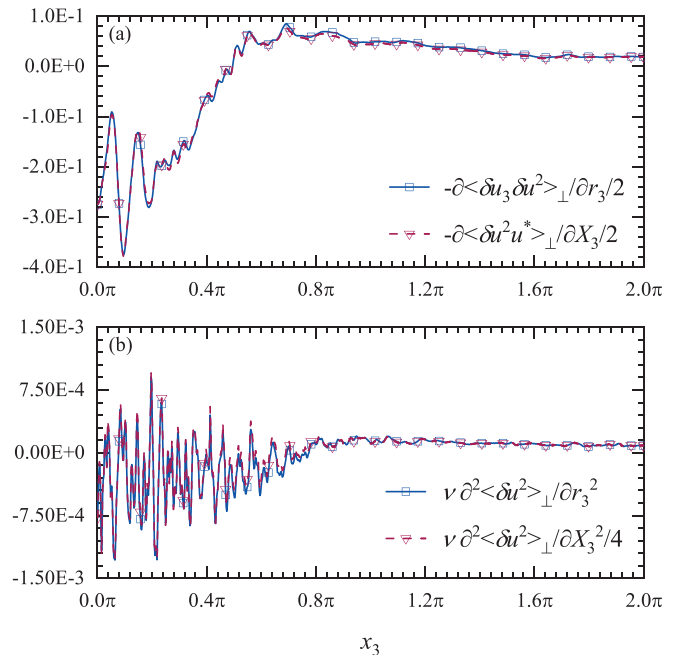


FIG. 9. Verification of the GKE. (a) The comparison of the turbulent convection term in r -space (only the component in the third direction) and geometrical space. (b) The comparison of the viscous diffusion term in r -space (only the component in the third direction) and geometrical space. The separation of the data $r = 0.48\pi$.

$$Q(r, x_3) = \frac{1}{N_{<r}} \sum_{r' < r} q(r', x_3) N_{r'}, \quad (31)$$

where $N_{<r}$ is the number of points with $|\mathbf{r}| < r$, and $N_{r'}$ is the number of points with $|\mathbf{r}| = r'$. By the average in the r -space, $\frac{1}{2} \langle \delta u^2 \rangle_{\perp}$ ($r = r_1, x_3$) can be interpreted as the mean scale energy of $r < r_1$. In addition, by the Gauss divergence theorem, the scale transports averaged in the r -space can be written as the fluxes from $r \geq r_1$ to $r < r_1$.³² Compared with the original definition, the r -space average can better depict the transport processes of scale.

Then, using the GKE [Eq. (26)] and neglecting the time derivative term, the average GKE can be written as

$$0 = T_g + T_r + V_g + V_r + T_p + C_p + P + D, \quad (32)$$

where T_g and T_r arise from turbulent convection in geometrical space and r -space, V_g and V_r relate to the viscous diffusion, T_p and C_p give the contributions of the pressure corresponding to the turbulent convection and the Coriolis force, P is due to production, and D represents the pseudo-dissipation. The scale transport process T_r and V_r can be divided into two components due to the directions of transports, respectively,

$$T_r = T_{r,\parallel} + T_{r,\perp}, \quad (33a)$$

$$V_r = V_{r,\parallel} + V_{r,\perp}, \quad (33b)$$

where $T_{r,\parallel}$ and $V_{r,\parallel}$ are the scale transports parallel to the rotating axis x_3 , $T_{r,\perp}$ and $V_{r,\perp}$ are the scale transports perpendicular to the rotating axis. Since only the separation \mathbf{r} with $r_3 = 0$ is considered, $T_{r,\perp}$ and $V_{r,\perp}$ act as fluxes, while $T_{r,\parallel}$ and $V_{r,\parallel}$ can be regarded as source terms.³⁴ For simplification, Eq. (32) is reorganized as

$$0 = T + T_{r,\perp} + V + C_p + P + D, \quad (34)$$

where the residual turbulent convection T and the viscous effect V can be written as

$$T = T_g + T_{r,\parallel} + T_p, \quad (35a)$$

$$V = V_{r,\perp} + V_{r,\parallel} + V_g + D. \quad (35b)$$

T includes all the terms related to the turbulent convection except $T_{r,\perp}$, and V represents all the effects associated with the viscosity.

All terms in Eq. (34) of case C is shown in Fig. 10. Figure 10(a) gives the results of $x_3 = 0.22\pi$ (in slowly rotating fields), and Fig. 10(b) shows the results of $x_3 = \pi$ (in fast rotating fields). First, in this figure, $T_{r,\perp}$ presents split energy transports (forward transports to small scales when $r < 0.14\pi$ and inverse transports to large scales when $r > 0.14\pi$ at $x_3 = 0.22\pi$), and its influence disappears when $r \rightarrow \infty$ ($r > 0.50\pi$ at $x_3 = 0.22\pi$). More importantly, at the separation $r \sim 10^{-2}$, $T_{r,\perp}$ at $x_3 = 0.22\pi$ is far larger than that at $x_3 = \pi$, which can be associated with the abundant small-scale structures with strong negative vorticity in Fig. 1(c). The interactions of the adjacent columnar vortices cascade energy to small scales, similar to rotating condensates.²⁴ In addition, the results show that $C_p > 0$ at $x_3 = 0.22\pi$ and $C_p < 0$ at $x_3 = \pi$, which represent that energy is transferred from fast rotating fields ($x_3 = \pi$) to slowly rotating fields ($x_3 = 0.22\pi$) by the Coriolis force. The effects of the residual turbulent convection T only appear at large separations ($r > 0.5\pi$). In contrast to C_p , $T < 0$ at $x_3 = 0.22\pi$ and $T > 0$ at $x_3 = \pi$, which are consistent with the results in Fig. 7.

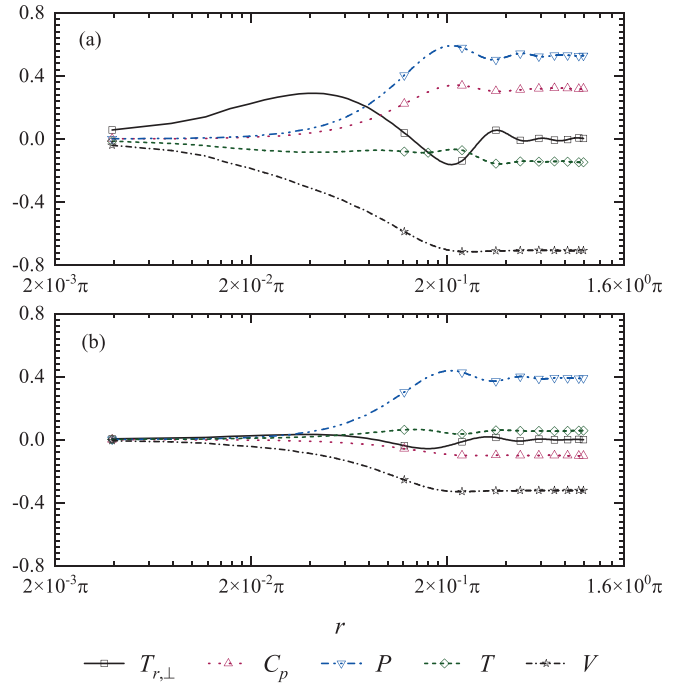


FIG. 10. All terms of the GKE vs the separation r of case C ($\alpha = 0.5$): (a) $x_3 = 0.22\pi$ and (b) $x_3 = \pi$. $T_{r,\perp}$: the turbulent scale convection perpendicular to the rotating axis; C_p : the pressure transport corresponding to the Coriolis force; P : the production; T : the residual turbulent convection; and V : the viscous effect.

The three components of the residual turbulent convection [Eq. (35a)] are shown in Fig. 11. As shown in the figure, T_g and $T_{r,\parallel}$ come to the same results at large scales [$r > 0.32\pi$ at $x_3 = 0.22\pi$ in Fig. 11(a), and $r > 0.24\pi$ at $x_3 = \pi$ in Fig. 11(b)], which is consistent with the asymptotic behavior in Eq. (29) and Fig. 9(a). Additionally, T_g and $T_{r,\parallel}$ both transfer energy from the slowly rotating fields to the fast rotating fields, in contrast to the Coriolis effects (C_p). T_p has opposite sign with the other two terms (T_g and $T_{r,\parallel}$), which reduces the spatial transport effects but not changes the transport direction of the overall turbulent convection effects (T). The four components of the viscous effect [Eq. (35b)] are shown in Fig. 12. $V_{r,\parallel}$ and V_g come to the same results at large scales, which is consistent with the asymptotic behavior in Eq. (30) and Fig. 9(b). Moreover, $V_{r,\parallel}$ and V_g are close to zeros at all separations r and positions x_3 , similar to the results in channel flows.³³ The pseudo-dissipation D is independent of the separation r . It is because that D is calculated by the sum at points \mathbf{x} and \mathbf{x}' , then averages over the $x_1 - x_2$ plane, which does not introduce the effects of the separation r . In addition, $V_{r,\perp}$ is always positive and transports energy from large scales to small scales, and the effect disappears at large separations ($r > 0.2\pi$).

In addition, in Figs. 10–12, all terms of GKE at $x_3 = 0.22\pi$ are larger than those at $x_3 = \pi$, which could be associated with the stronger turbulent strength and interaction of adjacent columnar vortices at $x_3 = 0.2\pi$. Furthermore, when $r > 0.08\pi$, the geometrical transport processes (T_g, T_p, C_p) and source terms ($T_{r,\parallel}, P, D$) play leading roles. However, in the inertial and dissipative region ($r < 0.08\pi$), only the scale turbulent convection $T_{r,\perp}$, the viscous scale transport $V_{r,\perp}$, and

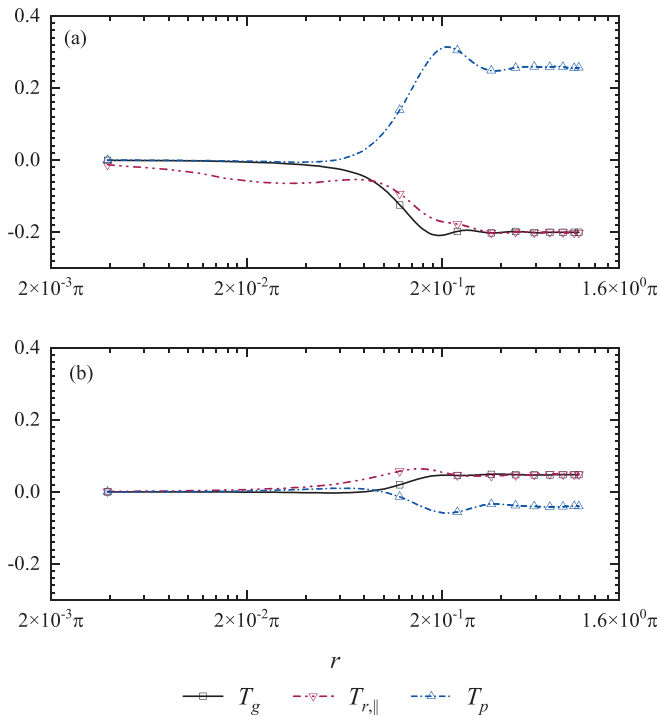


FIG. 11. The residual turbulent convection vs the separation r of case C: (a) $x_3 = 0.22\pi$ and (b) $x_3 = \pi$. T_g is the geometrical turbulent convection, T_p is the pressure transport T_p , and $T_{r,\parallel}$ is the scale convection parallel to the rotating axis.

the pseudo-dissipation D are significant. This is consistent with the traditional view of local isotropy.⁴⁷ In other words, small-scale behaviors are less affected by external effects.

V. VORTEX DYNAMIC PROCESSES

To further reveal the dynamic process, this paper studies the evolution of an axisymmetric columnar vorticity tube under inhomogeneous rotation. It should be noted that the definition of the vorticity tube is different from that of the vortex structure shown by the Q criterion in Fig. 1. The tangent line of any vortex filament on the tube is parallel to the direction of the vorticity, while the Q criterion addresses the magnitude of the vorticity. Since $E_{\parallel} = o(E_{\perp})$ in Fig. 4, it is reasonable to suppose that $u_{\parallel} = u_3 \approx 0$ and $\partial\Omega_3/\partial x_3 = \text{const} > 0$. At the beginning, $\partial E_{\perp}/\partial x_3 = \partial(u_1^2 + u_2^2)/\partial x_3/2 = 0$, $\omega_{\perp} = 0$ and $\omega = \omega_{\perp} + \omega_{\parallel} = \omega_{\parallel}$. The Coriolis force in the vorticity equation [Eq. (15)] can be decomposed as

$$2\nabla \times (\mathbf{u} \times \boldsymbol{\Omega}) \approx 2\mathbf{u} \frac{\partial\boldsymbol{\Omega}_3}{\partial x_3} + 2\boldsymbol{\Omega}_3 \omega_{\perp} \times \mathbf{e}_3 = \mathbf{F}_1 + \mathbf{F}_2, \quad (36)$$

where \mathbf{F}_1 is associated with the gradient of rotation, and \mathbf{F}_2 is related to the strength of rotation.

Figure 13 shows the evolution of a columnar vorticity tube. At first, $\mathbf{F}_2 = 0$, \mathbf{F}_1 is perpendicular to the vortex filament, which twists the columnar vortex and produces helicity ($H = \mathbf{u} \cdot \boldsymbol{\omega}$). Even though the vortex is twisted, the shape of the tube is unchanged at first. Then, $\omega_{\perp} \neq 0$ and $\mathbf{F}_2 \neq 0$. \mathbf{F}_2 faces toward the outer normal of the section, leading to section expansion and vortex shrinking. Then, $\boldsymbol{\omega}$ and \mathbf{F}_2

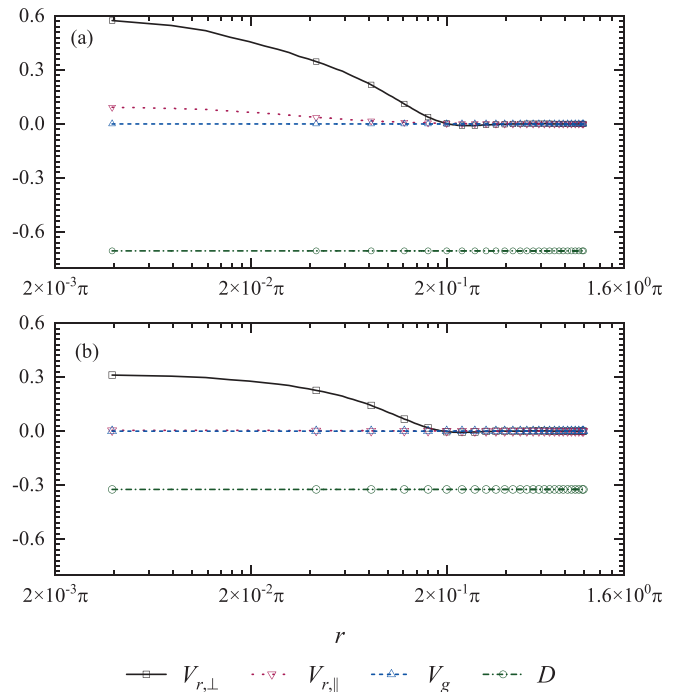


FIG. 12. The viscous effect vs the separation r of case C: (a) $x_3 = 0.22\pi$ and (b) $x_3 = \pi$. $V_{r,\perp}$ is the viscous diffusion perpendicular to the rotating axis, $V_{r,\parallel}$ is the viscous diffusion parallel to the rotating axis, V_g is the viscous diffusion in geometrical space, and D is the pseudo-dissipation.

rotate. Finally, ω_{\perp} faces toward the outer normal of the section, $\mathbf{F}_2 = -\mathbf{F}_1$, and helicity diminishes.

To conclude, the section of the columnar vorticity tube expands in the direction of $\partial\Omega_3/\partial x_3 > 0$. Considering the conservation of vorticity fluxes in the tube, the vorticity component ω_{\parallel} decays in the direction of $\partial\Omega_3/\partial x_3 > 0$. Furthermore, considering the axial symmetry and $u_{\parallel} = u_3 \approx 0$, it can be deduced that $\partial E_{\perp}/\partial x_3 < 0$. The analyses above qualitatively explain the dynamic process. The quantitative

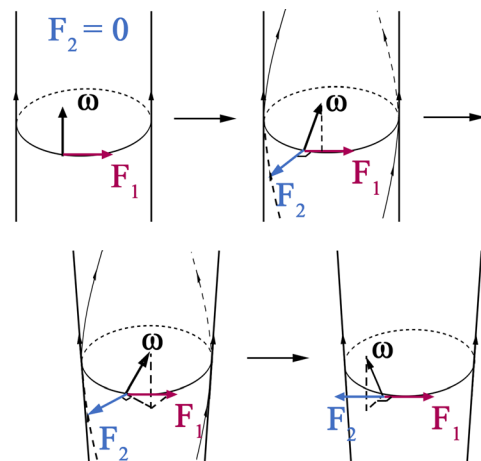


FIG. 13. Sketch of the evolution of a columnar vortex.

Downloaded from http://pubs.aip.org/aip/pof/article-pdf/doi/10.1063/5.0084098/1663667/035108_1_online.pdf

results can be obtained by the balance of \mathbf{F}_1 and \mathbf{F}_2 , which has been demonstrated by the linear prediction [Eq. (17)].

VI. CONCLUSIONS

In conclusion, in inhomogeneous rotating turbulence, energy is transferred to the slowly rotating fields by the Coriolis force. According to the linear analyses, the distribution of energy $\sim \Omega_3^{-2}(x_3)$, which has been verified by simulations. Moreover, the simulations showed that the normalized scale energy $\langle \delta \bar{u}^2 \rangle_{\perp} \sim \bar{r}^2$ in the dissipative region, $\langle \delta \bar{u}^2 \rangle_{\perp} \sim \bar{r}^{1.8}$ in the inertial region, and the distribution is geometrically self-similar. Compared with the homogeneous case, inhomogeneous rotation reduces the inverse cascades by linking the slow manifolds and other manifolds. Then, the transport process was studied in geometrical space and r -space simultaneously by the energy transport equation and the GKE. The asymptotic behaviors of the scale energy and GKE were analyzed theoretically and numerically. Moreover, the results of the GKE showed that the corresponding pressure of the Coriolis force transports energy from the fast rotating fields to the slowly rotating fields. Furthermore, the vortex structure and the GKE both revealed an extra energy scale transfer mechanism in the slowly rotating fields associated with the interference among adjacent columnar vortices, which is similar to the rotating condensate. Finally, we offered an intuitive physical interpretation for the spatial transport process by vortex dynamic analyses. The main effects of the Coriolis force on a vorticity tube can be decomposed into two components: one is associated with the gradient of rotation, and the other is related to the strength of rotation. The corresponding pressure of the Coriolis force transports energy to the slowly rotating fields by vortex shrinking and thickening. In the process, helicity appears at first and diminishes to zero in the end.

In this paper, we investigated several new phenomena and their intrinsic mechanisms associated with the inhomogeneous effects of the Coriolis force. It may help to understand the structures and dynamics of inhomogeneous rotating flows. Moreover, the introduction of inhomogeneity needs further theories different from traditional spectral analysis methods (such as the resonant wave theory⁴⁹).

ACKNOWLEDGMENTS

This work was supported by the National Key Research and Development Program of China (NKRDP) (Grant Nos. 2020YFA0711800, 2019YFA0405300, and 2016YFA0401200) and National Natural Science Foundation of China (NSFC) (Grant Nos. 91852203 and 12072349). The authors thank Beijing Super-Cloud Computing Center for providing computer time.

AUTHOR DECLARATIONS

Conflict of Interest

The authors have no conflicts to disclose.

DATA AVAILABILITY

The data that support the findings of this study are available from the corresponding author upon reasonable request.

REFERENCES

- ¹D. Yao, H. Xue, J. Yin, J. Sun, X. Liang, and J. Guo, "Investigation into the formation, structure, and evolution of an EF4 Tornado in East China using a high-resolution numerical simulation," *J. Meteorol. Res.* **32**, 157–171 (2018).

- ²J. Y. Cho, J. W. Skinner, and H. T. Thrastarson, "Storms, variability, and multiple equilibria on hot Jupiters," *Astrophys. J. Lett.* **913**, L32 (2021).
- ³H. Dumitrescu and V. Cardoso, "Rotational effects on the boundary-layer flow in wind turbines," *AIAA J.* **42**, 408–411 (2004).
- ⁴A. Alexakis and L. Biferale, "Cascades and transitions in turbulent flows," *Phys. Rep.* **767769**, 1–101 (2018).
- ⁵A. Tilgner, *Treatise on Geophysics* (Elsevier, 2007), pp. 207–243.
- ⁶J.-Z. Wu, H.-Y. Ma, and M.-D. Zhou, *Vortical Flows* (Springer, 2015), Vol. 28.
- ⁷R. H. J. Grimshaw, "A note on the β -plane approximation," *Tellus* **27**, 351–357 (1975).
- ⁸E. M. Edlund and H. Ji, "Nonlinear stability of laboratory quasi-Keplerian flows," *Phys. Rev. E* **89**, 21004–21004 (2014).
- ⁹A. S. Balbus, "When is high Reynolds number shear flow not turbulent?," *J. Fluid Mech.* **824**, 1–4 (2017).
- ¹⁰J. M. Lopez and M. Avila, "Boundary-layer turbulence in experiments of quasi-Keplerian flows," *J. Fluid Mech.* **817**, 21–34 (2017).
- ¹¹T. Gerkema, J. T. F. Zimmerman, L. R. M. Maas, and H. Van Haren, "Geophysical and astrophysical fluid dynamics beyond the traditional approximation," *Rev. Geophys.* **46**, 1–33, <https://doi.org/10.1029/2006RG000220> (2008).
- ¹²D. Su and H. Gao, "An exact solution for geophysical internal waves with underlying current in modified equatorial β -plane approximation," *J. Nonlinear Math. Phys.* **26**, 579–603 (2019).
- ¹³M. K. Sharma, M. K. Verma, and S. Chakraborty, "On the energy spectrum of rapidly rotating forced turbulence," *Phys. Fluids* **30**, 115102 (2018).
- ¹⁴M. K. Sharma, A. Kumar, M. K. Verma, and S. Chakraborty, "Statistical features of rapidly rotating decaying turbulence: Enstrophy and energy spectra and coherent structures," *Phys. Fluids* **30**, 045103 (2018).
- ¹⁵P. Maity, R. Govindarajan, and S. S. Ray, "Statistics of Lagrangian trajectories in a rotating turbulent flow," *Phys. Rev. E* **100**, 043110 (2019).
- ¹⁶S. K. Rathor, M. K. Sharma, S. S. Ray, and S. Chakraborty, "Bridging inertial and dissipation range statistics in rotating turbulence," *Phys. Fluids* **32**, 095104 (2020).
- ¹⁷L. M. Smith and F. Waleffe, "Transfer of energy to two-dimensional large scales in forced, rotating three-dimensional turbulence," *Phys. Fluids* **11**, 1608–1622 (1999).
- ¹⁸Q. Chen, S. Chen, G. L. Eyink, and D. D. Holm, "Resonant interactions in rotating homogeneous three-dimensional turbulence," *J. Fluid Mech.* **542**, 139–164 (2005).
- ¹⁹M. Buzzicotti, P. C. Di Leoni, and L. Biferale, "On the inverse energy transfer in rotating turbulence," *Eur. Phys. J. E* **41**, 131 (2018).
- ²⁰A. van Kan and A. Alexakis, "Critical transition in fast-rotating turbulence within highly elongated domains," *J. Fluid Mech.* **899**, A33 (2020).
- ²¹F. Waleffe, "The nature of triad interactions in homogeneous turbulence," *Phys. Fluids A: Fluid Dyn.* **4**, 350–363 (1992).
- ²²P. D. Mininni, A. Alexakis, and A. Pouquet, "Scale interactions and scaling laws in rotating flows at moderate Rossby numbers and large Reynolds numbers," *Phys. Fluids* **21**, 015108 (2009).
- ²³N. Yokoyama and M. Takaoka, "Energy-flux vector in anisotropic turbulence: Application to rotating turbulence," *J. Fluid Mech.* **908**, A17 (2021).
- ²⁴K. Seshasayanan and A. Alexakis, "Condensates in rotating turbulent flows," *J. Fluid Mech.* **841**, 434–462 (2018).
- ²⁵Y. Zhou, "A phenomenological treatment of rotating turbulence," *Phys. Fluids* **7**, 2092–2094 (1995).
- ²⁶P. K. Yeung and Y. Zhou, "Numerical study of rotating turbulence with external forcing," *Phys. Fluids* **10**, 2895–2909 (1998).
- ²⁷P. D. Mininni, D. Rosenberg, and A. Pouquet, "Isotropization at small scales of rotating helically driven turbulence," *J. Fluid Mech.* **699**, 263–279 (2012).
- ²⁸C. N. Baroud, B. B. Plapp, Z. S. She, and H. L. Swinney, "Anomalous self-similarity in a turbulent rapidly rotating fluid," *Phys. Rev. Lett.* **88**, 114501 (2002).
- ²⁹S. Galtier, "Weak inertial-wave turbulence theory," *Phys. Rev. E* **68**, 015301 (2003).
- ³⁰X. Yang and J. A. Domaradzki, "Large eddy simulations of decaying rotating turbulence," *Phys. Fluids* **16**, 4088–4104 (2004).
- ³¹R. J. Hill, "Equations relating structure functions of all orders," *J. Fluid Mech.* **434**, 379–388 (2001).
- ³²R. J. Hill, "Exact second-order structure-function relationships," *J. Fluid Mech.* **468**, 317–326 (2002).

- ³³N. Marati, C. M. Casciola, and R. Piva, "Energy cascade and spatial fluxes in wall turbulence," *J. Fluid Mech.* **521**, 191–215 (2004).
- ³⁴A. Cimarelli, E. De Angelis, and C. M. Casciola, "Paths of energy in turbulent channel flows," *J. Fluid Mech.* **715**, 436–451 (2013).
- ³⁵J. P. Mollicone, F. Battista, P. Gualtieri, and C. M. Casciola, "Turbulence dynamics in separated flows: The generalised Kolmogorov equation for inhomogeneous anisotropic conditions," *J. Fluid Mech.* **841**, 1012–1039 (2018).
- ³⁶B. Dubrulle, "Beyond Kolmogorov cascades," *J. Fluid Mech.* **867**, P1 (2019).
- ³⁷D. Gatti, A. Chiarini, A. Cimarelli, and M. Quadrio, "Structure function tensor equations in inhomogeneous turbulence," *J. Fluid Mech.* **898**, A5 (2020).
- ³⁸D. Morin, *Introduction to Classical Mechanics: With Problems and Solutions* (Cambridge University Press, 2008).
- ³⁹T. Pestana and S. Hickel, "Rossby-number effects on columnar eddy formation and the energy dissipation law in homogeneous rotating turbulence," *J. Fluid Mech.* **885**, A7 (2020).
- ⁴⁰D. R. Durran and C. Bretherton, "Comments on 'the roles of the horizontal component of the earth's angular velocity in nonhydrostatic linear models,'" *J. Atmos. Sci.* **61**, 1982–1986 (2004).
- ⁴¹P. A. Davidson, *Turbulence in Rotating, Stratified and Electrically Conducting Fluids* (Cambridge University Press, 2013).
- ⁴²M. K. Sharma, M. K. Verma, and S. Chakraborty, "Anisotropic energy transfers in rapidly rotating turbulence," *Phys. Fluids* **31**, 085117 (2019).
- ⁴³J. Pedlosky *et al.*, *Geophysical Fluid Dynamics* (Springer, 1987).
- ⁴⁴M. Buzzicotti, H. Aluie, L. Biferale, and M. Linkmann, "Energy transfer in turbulence under rotation," *Phys. Rev. Fluids* **3**, 034802 (2018).
- ⁴⁵E. Deusebio, G. Boffetta, E. Lindborg, and S. Musacchio, "Dimensional transition in rotating turbulence," *Phys. Rev. E* **90**, 023005 (2014).
- ⁴⁶P. A. Davidson, *Turbulence: An Introduction for Scientists and Engineers* (Oxford University Press, 2015).
- ⁴⁷A. N. Kolmogorov, "The local structure of turbulence in incompressible viscous fluid for very large Reynolds numbers," *Proc. R. Soc. London, Ser. A* **434**, 9–13 (1991).
- ⁴⁸Z. Yang, B. Q. Deng, B. C. Wang, and L. Shen, "Letter: The effects of stream-wise system rotation on pressure fluctuations in a turbulent channel flow," *Phys. Fluids* **30**, 091701 (2018).
- ⁴⁹F. Waleffe, "Inertial transfers in the helical decomposition," *Phys. Fluids A: Fluid Dyn.* **5**, 677–685 (1993).